PHYSICAL REVIEW A VOLUME 53, NUMBER 3 MARCH 1996

Numerical treatment of the time-dependent Dirac equation in momentum space for atomic processes in relativistic heavy-ion collisions

K. Momberger and A. Belkacem
Lawrence Berkeley National Laboratory, 1 Cyclotron Road, Berkeley, California 94720

A. H. Sørensen
Institute of Physics and Astronomy, University of Aarhus, DK-8000 Aarhus C, Denmark

(Received 5 September 1995)

A numerical method for the solution of the time-dependent Dirac equation to describe atomic processes in relativistic heavy-ion collisions is presented. Different from previous approaches found in the literature, we are working entirely in momentum space to propagate the electron wave function in time. Due to the localization of the electron in momentum space the wave function can be confined to a finite discretization volume without the stringent violation of the boundary conditions which is encountered in configuration-space methods. From the final state, we can extract probabilities on inner-shell ionization, excitation, electron transfer, and bound-free pair production. Results are presented in the energy range from 0.24 to 10 GeV/nucleon. At 0.24 GeV/nucleon we demonstrate that our formalism incorporates both the ionization and the transfer channel, which are equally important at this energy. At higher energies from 0.93 to 10 GeV/nucleon we focus on ionization and bound-free pair production. We find that the enhancement of bound-free pair production as compared to perturbation theory is much smaller than reported previously by others.

PACS number(s): 34.90.+q, 34.70.+e

I. INTRODUCTION

We present a theoretical study of atomic processes in relativistic heavy-ion collisions. The nuclear motion of the collision partners is treated classically and the interaction is assumed to be purely electromagnetic. The quantum-mechanical problem for the electronic motion is then governed by the time-dependent Dirac equation, which is coupled to the classical electromagnetic fields of the nuclei. The solution of this equation provides electron transition amplitudes for all nonradiative processes, such as ionization, excitation, and electron transfer. In addition to these conventional atomic physics processes electron-positron pair production can be described as ‘‘ionization from the Dirac sea.’’ An electron that initially occupies a state in the negative continuum can either get excited into a bound state of one of the ions or it may be emitted free. These processes are called ‘‘bound-free pair production’’ and ‘‘free-free pair production,’’ respectively. The produced vacancy in the Dirac sea describes the positron that escapes from the collision.

Since the number of heavy-ion facilities is quite limited, the amount of experimental work in this field is still relatively small. Ionization, excitation, and charge transfer have been investigated in a series of measurements by Anholt *et al.* [1–3] and Meyerhof *et al.* [4,5] using heavy-ion beams in the energy range of a few hundred MeV/nucleon. A few further experiments have been performed by other authors [6,7]. While inner-shell ionization, excitation, and charge transfer are well-known atomic physics processes, bound-free pair production has been observed only very recently at the Bevalac at the Lawrence Berkeley Laboratory [8,9]. This new ‘‘electron capture’’ from the Dirac sea is predicted to be the dominant source of beam loss in relativistic heavy-ion colliders like the Relativistic Heavy Ion Collider and Large Hadron Collider and, therefore, has attracted considerable interest in the recent years [10–20]. Measurements of free-free pair production using a highly relativistic sulfur beam have been performed at CERN [21].

Relativistic collisions of heavy ions are fundamentally different from those involving light ions, because the coupling constant of the perturbation can be large ($Z\alpha\approx0.6$) and the applicability of perturbation theory becomes questionable. Therefore, the theory of relativistic heavy-ion collisions may be regarded as a challenging testing ground for nonperturbative methods (for a general overview of the field, see [22–24]).

The perturbative approaches are based on the equivalent-photon method [22] and, to the largest part, on time-dependent perturbation theory, using a set of atomic wave functions attached to the target ion as basis functions for the electron or positron states [25]. Using distorted waves in a perturbation theory framework, Deco *et al.* included higher-order contributions of the Born series [26–28]. For simplicity, most authors chose approximate Sommerfeld-Maue wave functions for the continuum states and the corresponding Darwin wave functions for the bound states [22,26,29–32]. The exact Dirac wave functions have been used to describe ionization and pair production by Becker and co-workers [11,33–35] and recently by Baltz, Rhoades-Brown, and Weneser [36]. Electron transfer in relativistic collisions has been studied in a large variety of models, using both semirelativistic and exact relativistic wave functions (see [23,24]).

While it is still believed that perturbation theory in lowest order with a set of atomic basis states located at the target atom provides a correct description for small projectile charge numbers Z_P even for the heaviest targets, it became clear that this is no longer true in collisions with Z_P being large. For the case of ionization this became obvious from perturbation theory results at small impact parameters that exceed unity [37–39]. Also for free-free pair production in extremely relativistic heavy-ion collisions single-pair production probabilities can exceed unity [22,40,41].

The nonperturbative methods are based on a fully numerical solution of the time-dependent one-electron Dirac equation, so that the interaction with both nuclei ought to be included to all orders. These methods can be divided into two groups: the coupled-channel (or ‘‘close-coupling’’) methods, which are based on an expansion of the time-dependent wave function in a discrete set of basis states, and various grid methods, which tackle the Dirac equation by discretization on a spatial lattice. Due to the inherent limitation of the basis set, all coupled-channel calculations are highly dependent on the basis states being used in the expansion. However, they have been proven to be less numerically ‘‘delicate’’ and CPU-time intense than grid methods. Therefore, coupled-channel calculations have been used extensively with various choices for the basis functions, e.g., (i) two-center molecular states [42] to describe ionization and pair production, (ii) two-center atomic basis states to describe transfer and excitation [43–45], (iii) a set of one-center atomic states of the target, using a set of discrete wave packets as an approximation for the continuum to describe ionization, excitation, and bound-free pair production [17,38,46–48], and (iv) a set of free momentum space wave packets to describe free-free pair production [49,50].

Bound-free pair production has been the major point of interest of the work presented by Rumrich *et al.* [12] and Baltz, Rhoades-Brown, and Weneser [17,18]. The outcome of a coupled-channel calculation by Rumrich *et al.* exceeded the perturbation theory result for bound-free pair production by about 1–2 orders of magnitude at small impact parameters.

However, these authors have been criticized for using a relatively small basis set by Baltz, Rhoades-Brown, and Weneser [17,18], who claim that in a converged calculation this enhancement will get reduced to at most one order of magnitude at moderate relativistic collision energies and that it will not increase considerably the total cross section at ultrarelativistic energies.

With the advance of computer technology, grid calculations in relativistic atomic scattering theory have already become feasible today. For example, the finite-differences method and the finite-element method have been applied to the problem of ionization and pair production. Becker *et al.* [37,51] used a two-dimensional finite-differences method to compute ionization in almost central collisions and Thiel *et al.* [15] applied the same formalism to bound-free pair production. They report that their results exceed predictions by perturbation theory by 1–2 orders of magnitude. A two-dimensional finite-element code has been developed by Müller [52]. Wells *et al.* [53] applied a three-dimensional basis-spline collocation method to the problem of muonic bound-free pair production. Their results overshoot previous predictions in perturbation theory for comparable collision systems [54] by several orders of magnitude.

A common problem of these grid methods, which are all formulated in configuration space, is the fact that the electron density in configuration space dissolves during the collision [15,37] because of continuum components of the wave function that are arising due to the ionization and transfer reaction and ‘‘spread’’ over the whole configuration space. At the boundaries, however, the values of the wave function have to be set to zero. Therefore, the propagation in time has to be stopped, as soon as non-negligible components of the wave function are beginning to ‘‘hit the wall.’’

In this paper, we will present a method that removes the boundary condition problems to the largest part. We are solving the Dirac equation on a grid within a finite volume in momentum space, where the bound states as well as the continuum states are strongly localized [55]. The same is true for the time-evolved electron wave function. If the volume in momentum space is sufficiently large, the values of the wave function can, in a very good approximation, be set to zero at the boundaries of the grid. We are going to demonstrate that this formalism incorporates a description of inner-shell ionization, excitation, electron transfer, and bound-free pair production.

Common to all grid methods is the dilemma of finding a satisfactory treatment of the continuum. We are following the majority of the authors in this field [15,51,52] and use the analytically known solutions of the ‘‘continuous’’ problem, i.e., the Coulomb-Dirac eigenfunctions. This approach has been criticized because in a fully consistent grid calculation one ought to solve the eigenvalue problem of the discrete atomic Hamiltonian to compute a set of atomic eigenstates [56–58]. However, such states have not been satisfactorily implemented yet in a complete scattering calculation. Our choice of the Coulomb-Dirac wave functions is justified if the calculation is converged in the sense that a refinement of the grid will not critically affect the final results.

In the next section of this paper, we derive the time-dependent Dirac equation in momentum space and discuss the numerical implementation on two different parallel computers. In Sec. III, this method is applied to collision systems in the energy range from 0.24 to 10 GeV/nucleon. The technical details of the evaluation of the atomic states in momentum space are described in the Appendix.

II. THEORY

A. The Dirac equation

Let us assume the collision of a fully stripped projectile ion with charge Z_P on a target ion with charge Z_T, which is carrying only one electron in case we are considering ionization, excitation, or transfer or none in case of electron-positron pair production. Furthermore assuming pointlike charges and a straight line trajectory $\vec{R}(t)=(b,0,v_P t)$ for the projectile with constant velocity v_P the time-dependent Hamiltonian for one electron can be written as [23]

$$H_D = H_0 + V_P(t), \qquad (2.1)$$

where H_0 is the one-electron Hamiltonian corresponding to the target

$$H_0 = -i\vec{\alpha}\cdot\vec{\nabla} + \beta - \frac{Z_T e^2}{r}. \qquad (2.2)$$

Here, $\vec{\alpha}$ and β are the Dirac matrices [59]. $V_P(t)$ is the time-dependent perturbation by the projectile

$$V_P(\vec{r},t)=\frac{-Z_P e^2\gamma(1-v_P\alpha_z)}{\sqrt{(x-b)^2+y^2+\gamma^2(z-v_Pt)^2}}. \tag{2.3}$$

Natural units are used throughout the paper ($\hbar=m=c=1$); i.e., length will be measured in units of the reduced Compton wavelength $\lambda=\hbar/mc=386$ fm and momentum $p=\hbar k$ is measured in units of $\hbar/\lambda$. v_P denotes the projectile velocity and $\gamma=1/\sqrt{1-v_P^2}$ is the Lorentz factor. This expression for $V_P(t)$ can be derived from coupling the Liènard-Wiechert potential of a moving point charge [60] to the Dirac equation. To the atomic Hamiltonian H_0 belongs to a complete set of stationary hydrogenlike relativistic eigenstates $\phi_j(\vec{r})$ with

$$H_0\phi_j(\vec{r})=E_j\phi_j(\vec{r}). \tag{2.4}$$

In the somewhat naive picture of Dirac's hole theory, we have to think of the initial state as being given by the K-shell electron together with the initially fully occupied negative continuum ("Dirac sea") in the case of ionization, or of the fully occupied negative continuum only, in the case of pair production (for a formulation in terms of quantum electrodynamics, see [46] and [53]). We are going to neglect the electron-electron two-body interaction. Under this assumption, each electron state will evolve in time independently from all the others [61,62] according to the one-electron Dirac equation

$$i\frac{\partial}{\partial t}\psi_j(\vec{r},t)=[H_0+V_P(t)]\psi_j(\vec{r},t), \tag{2.5}$$

with the initial condition

$$\lim_{t\to-\infty}\psi_j=\phi_j e^{-iE_jt}, \tag{2.6}$$

while orthogonality and completeness are preserved during the collision. We still have to deal with an infinite number of electrons. After introducing a wave packet approximation for both continua, one can in fact propagate each state and compute any desired many-particle transition amplitude, as has been done for correlated one-pair electron-positron pair production [14,49]. The many-particle amplitudes can be expressed in terms of one-electron amplitudes. In case we are interested only in the *total* probabilities for ionization or pair production, these very complicated expressions can be reduced to simple incoherent sums of the one-electron transition probabilities [46,53]. For example, the total probability to observe an electron from bound-free pair production is given by

$$P_{\mathrm{bfpp}}=\sum_{E<-m_0c^2}|\langle\phi_{1s}|\psi_E(\infty)\rangle|^2 \tag{2.7}$$

and the probability to observe a K-shell vacancy from K-shell ionization is

$$P_{\mathrm{ioniz}}=\sum_{E>m_0c^2}|\langle\phi_E|\psi_{1s}(\infty)\rangle|^2. \tag{2.8}$$

To simplify the calculation of P_{bfpp} we make use of the time-reversal rule $|\langle\phi_i|\psi_j(\infty)\rangle|^2=|\langle\phi_j|\psi_i(\infty)\rangle|^2$, which is fulfilled due to the assumption of a straight line projectile trajectory [46]. This enables us to compute P_{ioniz} and P_{bfpp} by only propagating the 1s state. Projection of the final state onto the positive and negative continuum states will yield the probabilities for ionization and bound-free pair production, respectively.

B. The transformation to momentum space

In this section, we will derive a time-dependent integral equation for the Dirac equation in momentum space. We define the Fourier transformation of the time-dependent spinor $\psi(\vec{r},t)$ as

$$\psi(\vec{r},t)=\frac{1}{(2\pi)^{3/2}}\int d^3k\,\tilde{\psi}(\vec{k},t)e^{i\vec{k}\cdot\vec{r}}. \tag{2.9}$$

Insertion into the Dirac equation (2.5), multiplication by $[1/(2\pi)^{3/2}]\exp(-i\vec{k}'\vec{r})$ and integration over $\vec{r}$ yields

$$\frac{\partial}{\partial t}\tilde{\psi}(\vec{k},t)=\frac{-i}{(2\pi)^3}\int\int d^3k'\,d^3r\,e^{-i\vec{k}\cdot\vec{r}}\times[H_0+V_P(t)]e^{i\vec{k}'\cdot\vec{r}}\tilde{\psi}(\vec{k}',t). \tag{2.10}$$

The three-dimensional Fourier integral over the Coulomb potential is known as the Bethe integral [25,63,74]:

$$\int d^3r\,e^{i\vec{q}\cdot\vec{r}}\frac{1}{r}=\frac{4\pi}{q^2}. \tag{2.11}$$

Making use of this equation we can perform the r integral in Eq. (2.10) and obtain the following integral equation for the Dirac equation in momentum space:

$$\begin{aligned}\frac{\partial}{\partial t}\tilde{\psi}(\vec{k},t)=&-i[\vec{\alpha}\cdot\vec{k}+\beta]\tilde{\psi}(\vec{k},t)+\frac{-i}{2\pi^2}\int d^3k'\\&\times\left[-\frac{Z_Te^2}{q^2}\right]\tilde{\psi}(\vec{k}',t)+\frac{-i}{2\pi^2}\int d^3k'\\&\times\left[\frac{-Z_Pe^2(1-v_P\alpha_z)e^{i(q_xb+q_zv_Pt)}}{(q_x^2+q_y^2+q_z^2/\gamma^2)}\right]\tilde{\psi}(\vec{k}',t),\end{aligned} \tag{2.12}$$

where $\vec{q}=\vec{k}'-\vec{k}$ denotes the momentum transfer. This equation of motion has to be solved with the initial condition:

$$\lim_{t\to-\infty}\tilde{\psi}(\vec{k},t)=\tilde{\psi}_{1s}(\vec{k},t). \tag{2.13}$$

The expressions for the initial state are derived in the Appendix. In the next section we will describe how Eq. (2.12) is treated numerically.

C. Numerical treatment of the time evolution and computational details

The numerical method to perform the time integration of (2.12) is based on the following idea: First, we enclose the system in a finite volume in momentum space. In momentum space, we expect the wave function to be well localized for all times during the collision, so that the values at the surface of the volume can be set to zero or to some small constant value for all times during the collision. The assumption that the wave function will be well localized has to be checked at all times during the collision. In the next step, we discretize the problem by introducing a grid within this volume. The grid has been defined in spherical and—in another version of the code—in cylindrical coordinates, as we will describe later in more detail. The wave function itself is represented within the whole volume by defining a global three-dimensional (3D) interpolating function on the grid. This interpolating function is constructed from a two-dimensional cubic spline in k and θ_k (in the case of spherical coordinates, or $k_\perp=\sqrt{k_x^2+k_y^2}$ and k_z in case of cylindrical coordinates), which is followed by a quadratic Lagrangian interpolation [64] in the azimuthal angle ϕ_k. This is supposed to be less accurate than a fully three-dimensional spline function, but requires less CPU time and memory and has been found to work well. Before the interpolation is carried out, the wave function is multiplied by a weight function $w(q)$ given by

$$w(q)=1+[1-\exp(-\eta q)]q^{(E_{1s}+2)}, \tag{2.14}$$

which behaves reciprocal to the asymptotic of the initial 1s state and converges to one for $q\to 0$. The parameter η has been set to 0.75. This choice of the weight function substantially improves the quality of the interpolation.

Once the interpolating function is provided, we can evaluate the momentum space integral in Eq. (2.12) by means of Gaussian quadrature, as we will explain later in more detail.

Let us first have a closer look at what the discretization does. We rewrite the Dirac equation in momentum space in the following general way:

$$\frac{\partial}{\partial t}\tilde{\psi}(\vec{k},t)=F_1(\vec{k})\tilde{\psi}(\vec{k},t)+\int d^3k' F_2(\vec{q},t)\tilde{\psi}(\vec{k}',t), \tag{2.15}$$

where F_1 denotes the term in Eq. (2.12) that comes from the free Dirac Hamiltonian and F_2 stands for both of the q-dependent kernels of the integral terms in Eq. (2.12), describing the interaction of the electron field with the target and the projectile, respectively. Discretization means that the continuous variable $\vec{k}'$ goes over into a set of grid points in spherical (cylindrical) coordinates:

$$\vec{k}'=\vec{k}_j'=(k_j',\theta_j',\phi_j'),\quad j=1,(1),N, \tag{2.16}$$

where N is the maximum number of grid points. A spinor function $\tilde{\psi}(\vec{k}',t)$ with 8 real components is attached to each point $\vec{k}_j'$:

$$\tilde{\psi}(\vec{k}',t)\to\tilde{\psi}(\vec{k}_j',t)=:\tilde{\psi}_j(t). \tag{2.17}$$

The continuous equation of motion in momentum space (2.15) now goes over into a set of coupled differential equations of the general form

$$\frac{d}{dt}\tilde{\psi}_j=F_1(\vec{k}_j)\tilde{\psi}_j(t)+\sum_i F_2(\vec{k}_i'-\vec{k}_j,t)\tilde{\psi}(\vec{k}_i',t)w_i. \tag{2.18}$$

Here, w_i and $\vec{k}_i'$ stand for the weights and abscissas of a three-dimensional quadrature over the whole k space. Note that the right-hand side of the system of differential equations (2.18) is nonlinear. Note further that as many momentum space integrals have to be solved as we have grid points in momentum space. There are two characteristics of the integral kernel F_2 that make the numerical quadrature quite cumbersome, namely, (i) a quadratic singularity at $q=0$ and (ii) oscillations of the projectile term along $\vec{R}=(b,0,v_pt)$.

We solved the momentum space integral by slicing the integration volume into cells, which were adjusted to the behavior of the integrand. The integration is performed cell by cell using three-dimensional Gaussian quadrature techniques. In more detail, the way we slice momentum space in cells depends on the underlying hardware being used for the computation. We used two different kinds of parallel machines, which required totally different programming and integration techniques. First, we have run our computer code on a cluster of (up to ten) SUN Sparc 10 workstations (providing a peak performance of 170 Mflops), running the software package PVM (parallel virtual machine), which allows an eventually heterogeneous computer network to be used as a virtual parallel computer with distributed memory. Our computer code is organized according to the master-slave model. The ‘‘master’’ contains input and output, bookkeeping, and the time-integration routine and is running on one of the processors (*host*), while the ‘‘slave’’ contains the momentum space quadrature code and is running as identical copies on all the other processors (*nodes*). PVM allows for the message passing between the host process and all the node processes, especially copying the vector $\tilde{\psi}_j(t)$ from the host to each node and returning the values of the derivative vector $d_t\tilde{\psi}_j(t)$ in small packages from the hosts to the node. The integration volume itself is defined to be a large sphere with a radius of typically $10.0[1/\lambda]$. This volume encloses about 99.9% of the norm of the initial wave function and has been found to be sufficiently large in a collision energy range from 0.24 to 10 GeV/nucleon. Within this sphere, we defined a grid in spherical coordinates (k,θ_k,ϕ_k) with $(13\times 7\times 10)$ points, respectively, using a logarithmic distribution in k and an equidistant spacing in the angles. The 2D spline interpolation is defined on the 10 (k,θ_k) planes, while we use quadratic interpolation in ϕ_k to calculate the values in between. Since these processors provide a sufficient amount of memory, we can perform the whole momentum space integral on each processor. In order to perform the integral over the sphere, we embed the whole sphere in a cylindrical integration volume. This cylindrical volume is sliced into smaller cells with a given thickness in Δk_z and $\Delta k_\perp$ and angular segment $\Delta\phi_k$. The thickness in k_z is adjusted to the time-dependent wavelength of the oscillation given by $\vec{R}=(b,0,v_pt)$. The cells that are neighboring the singularity are integrated with higher accuracy than the rest. Since the integration volume is larger than the sphere that contains the time-dependent wave function, we have set the values of the wave function outside the sphere equal to the values of the 1s ground-state wave function, just to give it some well-defined nonzero values. This is an assumption that has been found to work well.

Thus, we are provided with a method to compute the right-hand side of the system of differential equations (2.18). In the next step, we have to perform the time integration, which is done on the host. We use a fourth-order Zonneveld-Adams-Moulton predictor corrector method (in the PECE scheme), which uses a Runge-Kutta-type formula (Zonneveld formula) for the start calculation [65]. This routine is run with fixed step size of typically 0.05, in order to have a good estimate of the CPU-time requirements. The CPU time for one time integration at a given impact parameter running PVM was up to several hundred hours.

On a later stage of this project, we moved our code to a MasPar MP2, which is a massively parallel computer being equipped with 4096 processors that provides a peak performance of 1.6 Gflops. However, the MasPar system architecture imposes some severe restraints on the code structure. Memory on the MasPar MP2 is limited to 64 kbyte for each processor, so that it is impossible to store the spline coefficients for the whole wave function in each processor. Therefore, we had to redesign the momentum space integration routine. First, we decided to get rid of the spherical grid and define a cylindrical volume that contains the time-dependent wave function on a grid in cylindrical variables $(k_\perp, k_z, \phi_k)$, so that the volume in which the time-dependent wave function is defined and the integration volume are identical. As before, we split this volume into smaller cells, where the corners of these cells are given by the points of the grid, i.e., the cells are defined independently of time now. This allows for a one-to-one mapping between each cell of the momentum space and each processor of the MasPar processor element array. Each processor has to store only the spline coefficients for one of the cells in memory. To obtain the result of a whole momentum space integral, we simply have to perform a summation over the MasPar processor element array. We have to perform as many such integrations, as we have grid points in k space. In order to match approximately the dimensions of the 64×64 processor element array, we have chosen a grid of $(12\times24\times14)$ points in cylindrical coordinates $(k_\perp, k_z, \phi_k)$ with a logarithmic spacing in $k_\perp$ and k_z. The MasPar allows us to perform a whole time integration within a minimum of 30 h with a much finer grid compared to the PVM runs. A further important advantage of the MasPar over PVM is the much better reliability and stability of the system.

In yet another version of the computer code, we restricted ourselves to almost central collisions (the impact parameter is actually set to zero) so that we can assume rotational symmetry of the collision system. In this case, the time evolved state will maintain the trivial ϕ_k dependence of the initial 1s state, so that we can reduce the grid to two dimensions $k_\perp$ and k_z with (32×128) points. The quality of the numerical results in this 2D calculation clearly excels the 3D results. This indicates that in future work the 3D calculations should be further refined.

III. APPLICATIONS AND RESULTS

We illustrate different features of our method by studying collision systems at various projectile energies in the range from 0.24 up to 10 GeV/nucleon for a gold projectile and a uranium target. We will focus our discussion on different processes as the energy varies. The energy of 0.24 GeV/nucleon has been chosen to highlight the transfer process. At this energy, the projectile velocity corresponds to the classical velocity of a bound electron in the K shell of the target ion (‘‘matching energy’’ [23]), so that charge transfer is expected to be large. At higher energies, ranging from 0.93 to 10 GeV/nucleon, transfer is small and we will concentrate on the behavior of the ionization and the bound-free pair production process. Most of these examples have been performed with the MasPar using the ‘‘fine’’ grid at zero impact parameter. To show the effect of nonzero impact parameters, this section also includes an impact parameter study for the collision system at 0.93 GeV/nucleon and values for total cross sections. Results for ionization and bound-free pair production will be compared with predictions in first-order perturbation theory, which have been obtained using the perturbation theory codes provided by Becker [46].

A. Study of a ‘‘low’’-energy collision at 0.24 GeV/nucleon

1. Time evolution in momentum space

In Fig. 1 we display the time evolution of the electron density in momentum space $\tilde{\psi}^\dagger(k)\tilde{\psi}(k)$ for a collision at 0.24 GeV/nucleon ($\gamma=1.259$) and impact parameter $b=0$. This is a result of a MasPar run with the ‘‘fine’’ grid of 128×32 points in k_z and $k_\perp$. The density is shown on a linear scale in a square region of the k_x-k_z plane, ranging from -3 to $+3$ in both coordinates (note that the calculation was actually performed within a cylindrical volume with a length and diameter of 20 units). In configuration space, the projectile is traveling along the z axis. As is obvious from this figure, the electron density remains localized nearby the origin at all times. Different from the situation in configuration space, we do not observe a ‘‘spread’’ of the wave function over the whole grid and the change of the wave function at the boundaries remains negligible. The time propagation has been performed from $t=-30$ to $+20$. The wave function is displayed at time $t=-5$, 0, 5, 10, 15, and 20. At larger negative times, the changes of the wave function are not very drastic. At $t=-5$ it is still very close to the density of the initial 1s state, however, we find it to be slightly shifted in the direction of the incoming projectile, which means that the electron gets accelerated towards the projectile. Around $t=0$ the electron density looks as if it is strongly localized around the center, meaning that the electron has reacted to the combined charge of the projectile and target. At positive times, we can observe strong excitation and ionization processes coming up. For $t>5$ we notice that the maximum of the electron density is localized around $k_z=0.76$. This value of the momentum corresponds to the momentum of a free electron moving with the same γ value as the projectile ion. We observe circular continuum waves that are centered around the momentum of the projectile. These waves can be interpreted as continuum states in the projectile frame, describing ‘‘capture to the continuum of the projectile.’’

The wave function at $t=+20$ has been projected onto the target states and the projectile bound states. We found only 3.5% in the target 1s state and 7.3% in the higher target bound states. By projection onto the projectile bound states, we found about 31.4% for the projectile 1s state and 3.3%

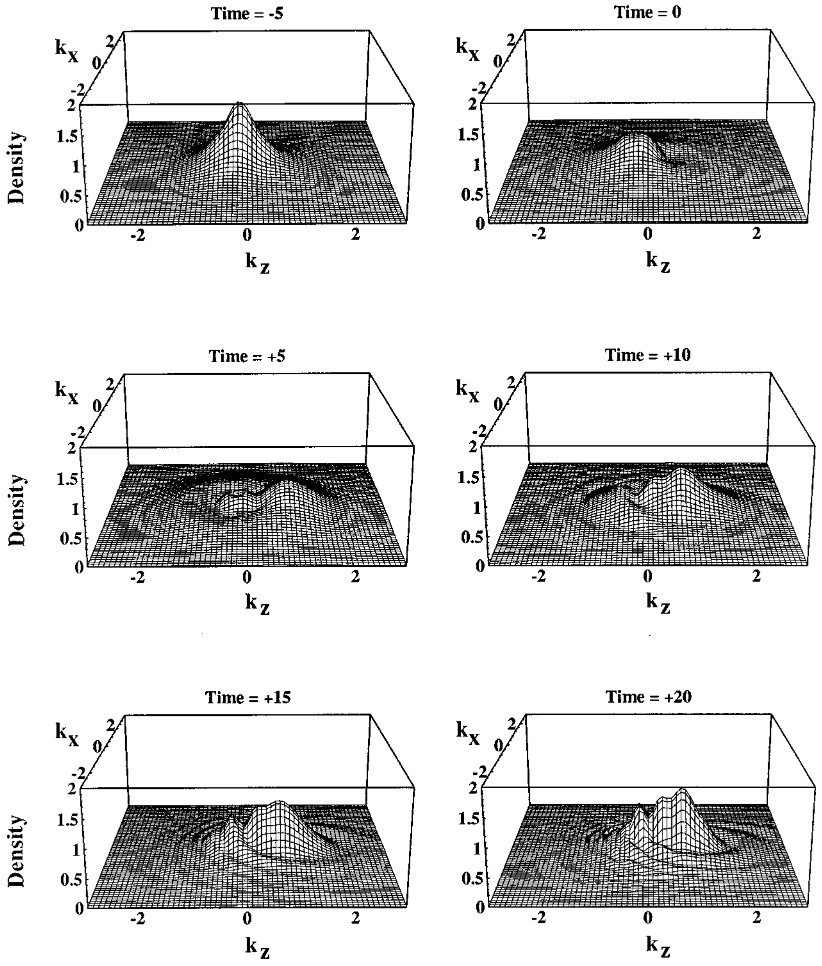

FIG. 1. Time evolution of the momentum space density in the collision system Au + U at E_{lab}= 0.24 GeV/nucleon and impact parameter zero.

for the L shell. For the projection onto the continuum states we followed the procedure outlined in the Appendix. The angular momentum summation has been extended to up to $|\kappa| = 10$, while the energy integration was typically extended over the interval from $|E| = 1.05$ to 5.05 for both the positive and negative continuum. The projection on the negative continuum amounts to about 2×10^{-3}. The overlap with the positive continuum states of the target amounts to more than 89%. These values are to be compared to the perturbation theory predictions of 94.4% for the positive continuum and 1.95×10^{-5} for the negative continuum, respectively.

Special care has to be taken in the interpretation of these projections. In any case, the projection on the positive continuum can be interpreted as the probability for electron removal from the target ion. However, since the projectile bound states are nonorthogonal to the complete set of target states, we are counting the components found in the projectile bound states twice, once as transfer probability and once as probability for a transition within the set of target states, so that we end up with a total transition probability larger than 100%. As shown in the Appendix (Sec. 2 b), the inner-shell states of the projectile are at larger times predominantly overlapping with the positive continuum states of the target, while the overlap with the negative continuum is small and the overlap with the bound states of the target is practically negligible. That means that in particular the projections on the positive and negative continua have to be corrected for the contributions from the projectile bound states. We are doing this by subtracting the projectile bound states coherently, weighted by their amplitudes, from the time-evolved state. After subtraction of the K- and L-shell projectile states we obtain a corrected value for ionization of 55% and a value of 2×10^{-4} for bound-free pair production. The latter value exceeds perturbation theory by one order of magnitude.

The time evolution of the projections on the 1s state, the higher target bound states (up to the N shell), the positive continuum (corrected for K-shell transfer), and for the K-shell transfer are shown in Fig. 2. Only the asymptotic values for time $t \rightarrow \infty$ are physically meaningful, since the projection on the target states cannot be interpreted as transition probabilities while the projectile field is still present. The time evolution is shown here, because this allows for a comparison with the previous calculations in the coupled channel and finite-differences method. Apparently, the transfer probability is perfectly converged, while ionization and the target 1s state are still slightly increasing and the excitation is decreasing. For reasons of CPU-time limitations, the time propagation has been stopped here.

To illustrate the subtraction procedure we show in Fig. 3 (a) the density of the projectile bound states of the K and L shells taken at time $t = +20$ (being summed up coherently with the amplitudes that have been found in the projection)

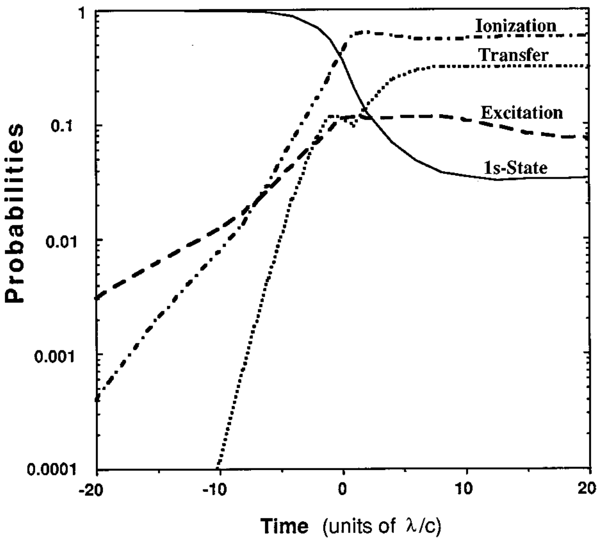

FIG. 2. Time evolution of the occupation probabilities for the collision system Au + U at $E_{\mathrm{lab}}=$ 0.24 GeV/nucleon obtained by projection on the various sets of target and projectile states. The ionization probability has been corrected for transfer by subtraction of the K- and L-shell projectile states, as explained in the text.

and (b) the state obtained by subtraction of (a) from the state displayed in Fig. 2 at time $t=+20$.

After the subtraction we find the maximum of the density distribution at the origin. The relative maxima around $k_z=-0.2$ and $k_z=+0.3$ that can be observed in Fig. 1 at time $t=20$ have disappeared. A small peak remains at $k_z=0.76$, which we ascribe to even higher projectile bound states and continuum components traveling with the speed of the projectile.

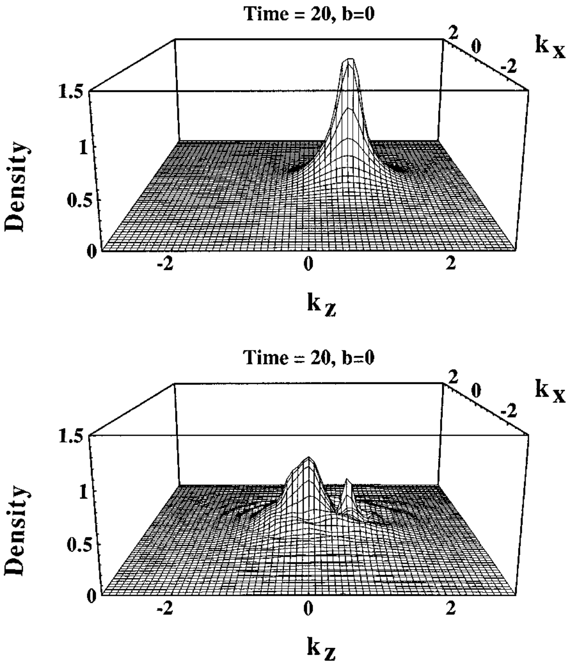

FIG. 3. Coherent sum of the K- and L-shell projectile states (weighted with their complex amplitudes) (a) and the distribution obtained by subtraction of these states from the wave function at time $t=+20$ shown in Fig. 1(b).

2. Fast Fourier transformation to configuration space

In order to support the interpretations of the results for the various processes that have been presented in the previous section, we performed a fast Fourier transformation (FFT) of $\tilde{\psi}(\vec{k},t)$ to obtain $\psi(\vec{r},t)$ in configuration space, using the MATHEMATICA environment (for details about FFT, see, e.g., [66] and [67]). For the FFT we have chosen a Cartesian grid in k_x and k_z, ranging from -3 to $+3$ in each variable with a step size of 0.1. This grid in k space corresponds to a reciprocal lattice in configuration space. The boundaries of the reciprocal lattice are related to the grid in k space by $z_{\max}=2\pi/\Delta k_z$ and $\Delta z=\pi/k_{\max}$. In our case, this means that the grid in configuration space extends from -10π to $+10\pi$ in x and z with a step size of $\pi/3$. The time evolution of the density in *configuration* space is displayed in Fig. 4 on a logarithmic scale. At time $t=20$ the density distribution has its global maximum around the position of the projectile (at $v_p t=0.60755\times 20=12.15$) and is surrounded by a large well of continuum waves, which have partially passed the projectile and are mainly going into the forward direction. Another local maximum is found around the origin, corresponding to the target bound states. The final state at $t=+20$ is highlighted in Fig. 5 on a linear scale, in order to emphasize that this structure in configuration space is strongly peaked, while it is smooth in momentum space. This is due to the fact that the bound-state wave functions in configuration space are singular around the origin, while they are regular in momentum space (see Appendix, Sec. 2 b).

This figure demonstrates clearly that the configuration-space wave function spreads proportionally to the time t and therefore a much larger volume would be necessary to fully enclose the wave function within a given time range, as compared to momentum space. Additionally, the sharp peak structures around the target and the projectile are very hard to describe on a mesh in configuration space.

B. Study of higher energetic collisions at (0.93–10) GeV/nucleon

In this section, we will move to higher energies and focus our discussion on the behavior of ionization and bound-free pair production. In particular, we will put a strong emphasis on a comparison of our data for bound-free pair production to the results in perturbation theory and comment on the "nonperturbative enhancement effect" that has been claimed by several authors [12,14,17,18].

1. Time evolution of the collision system at 0.93 GeV/nucleon

Let us investigate first the collision system Au + U at $E_{\mathrm{lab}}=0.93$ GeV/nucleon ($\gamma=2$), which is shown at several time steps ranging from -5 to $+20$. For Fig. 6, we have also chosen impact parameter $b=0$, which has been run on the MasPar with the "fine" grid. Although the general features at negative times are quite similar to the previous example, the situation is remarkably different at positive times. The transfer peak, which at this energy should be located at $k_z=1.4$, is not visible anymore. Unlike the previous example, where

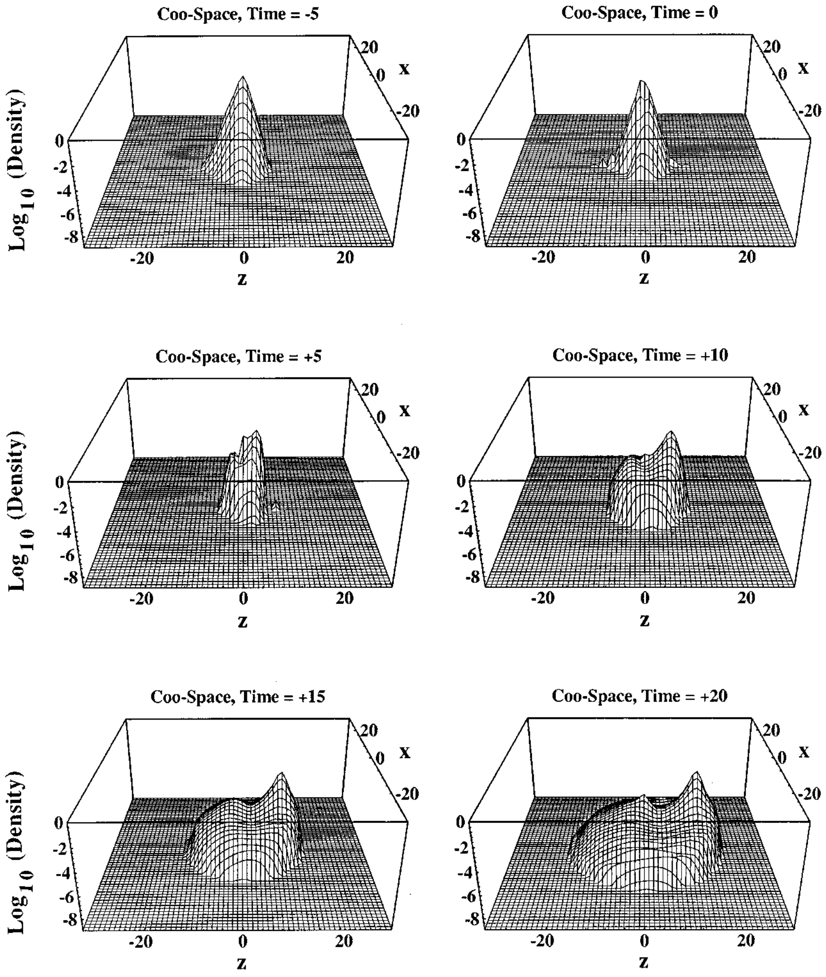

FIG. 4. Time evolution of the configuration space density on a logarithmic scale corresponding to the collision system shown in Fig. 1, obtained by FFT.

transfer was dominant, we find the global maximum of the density at the center of the coordinate system. We observe circular continuum waves of higher momentum centered around the origin. Note that the grid lines are rectangular in the k_x-k_z plane and that no grid related structures are visible.

For a further comparison with the previous example, we performed the FFT with the same method and grid parameter settings as before. In Fig. 7 we display the configuration-space density of this collision system taken at time $t=+20$ on a logarithmic scale. We find a strongly dominant maximum at the center of the coordinate system, surrounded by a very broad distribution of continuum components that are traveling outward. About 30° from the forward direction a sharp ridge sitting on the broad background of continuum states can be observed, which is traveling with about the same speed as the transfer peak. At this collision energy, the transfer peak is not passed by continuum waves, as had been found in Fig. 4, since its velocity is close to the speed of light.

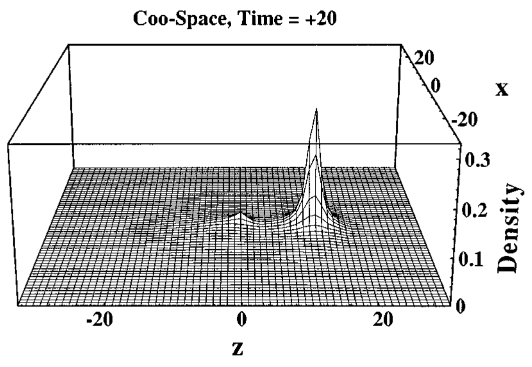

FIG. 5. Configuration-space density for the collision system in Fig. 4 taken at time $t=20$ on a linear scale.

In the next step, we analyzed the time evolved states from Fig. 6 by projection onto the various sets of target states to obtain the probabilities for inner-shell ionization, excitation, and bound-free pair production. Results are displayed in Fig. 8. The figure shows the probabilities for the initial 1*s* state (which is starting at 100%), *K*-shell ionization, excitation, and bound-free pair production. We find that the initial 1*s* state gets strongly depleted around $t=0$ and converges rapidly to a final value of about 29.5%. The final value for excitation to higher bound states amounts to 9.8%. We find that the final excitation probabilities for the higher shells exhibit a $1/n^3$ behavior. The final value for *K*-shell transfer, which is not displayed in this figure, amounts to 2.5%.

The projection onto the positive continuum reaches a maximum value of about 61% at time $t=+10$ and is going down at larger times to about 54.3%. For the bound-free pair production we find the typical behavior, which is already well known from coupled channel calculations, that it even-

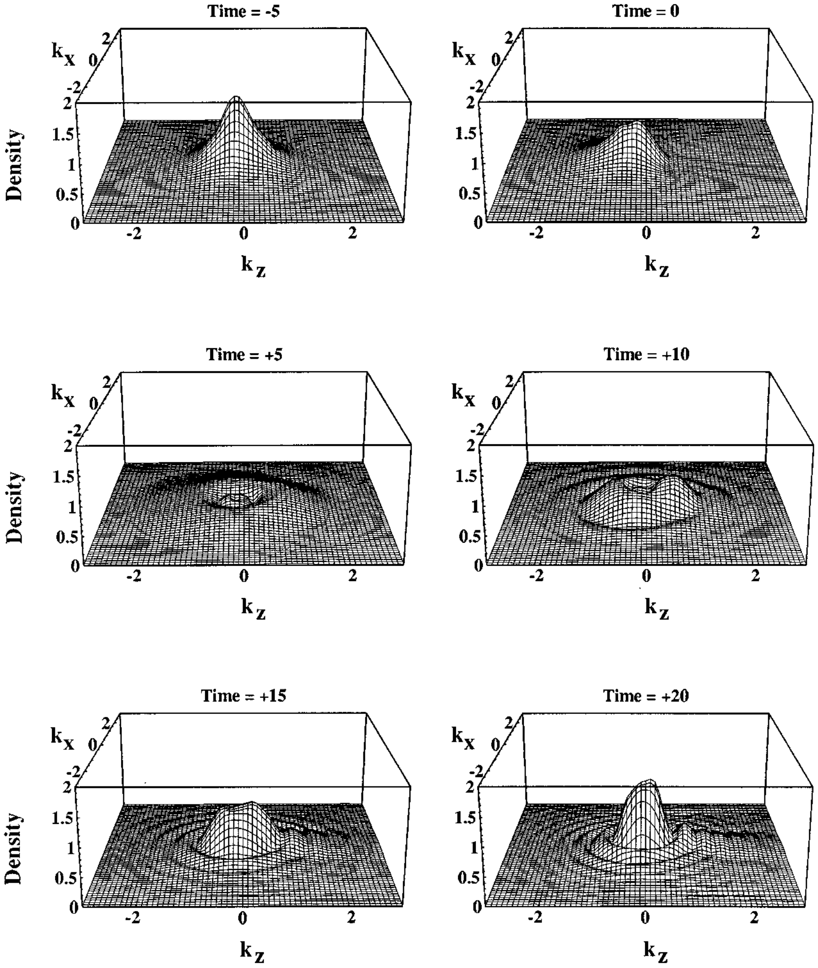

FIG. 6. Time evolution of the momentum space density shown in the collision system Au + U at 0.93 GeV/nucleon and impact parameter zero.

tually reaches very high values of the order of several percent around $t=0$ and drops by orders of magnitude at larger positive times. Here, it converges to a final value of 3.9×10^{-4}, which is about 4.4 times larger than the perturbation theory value of 0.89×10^{-4}. The correction of this value with respect to the overlap of the projectile 1*s* state (charge transfer) leads to a further reduction of this value by about 10%. We do not consider this correction as significant and, therefore, it has not been included in this figure. In Fig. 9 we show the energy distributions obtained by the projections on the positive and negative continua in comparison to the perturbation theory results. This figure shows that the enhancement of bound-free pair production comes mainly from positrons with a kinetic energy less than 1 mc^2.

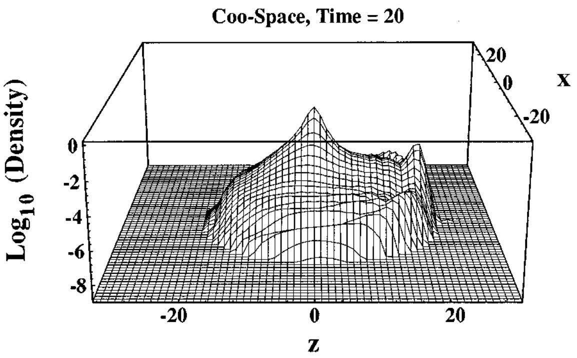

FIG. 7. Configuration-space density obtained by FFT for the collision system shown in Fig. 6 at time $t=20$ on a logarithmic scale.

The result for bound-free pair production contradicts the predictions of a strong “nonperturbative enhancement of bound-free pair production” of typically more than an order of magnitude being found in coupled-channel calculations for similar collision systems [12]. Although all the arguments about the nonapplicability of perturbation theory given in [12] and [39], in first place the violation of unitarity in perturbation theory, still hold, we suspect that this enhancement effect has been overestimated due to the restricted atomic basis sets being used in these calculations.

2. Time evolution of the collision system at 10 GeV/nucleon

To demonstrate that this formalism can be extended to higher γ values, we finally present results for the system Au+U at $E_{\mathrm{lab}}=10$ GeV/nucleon ($\gamma=11.7$) and impact parameter $b=0$ using the two-dimensional “fine grid” on the MasPar. The time integration has been performed from $t=-20$ to $+20$. The time evolution of the momentum space density is shown in Fig. 10 at times $t=-5$, 0, 5, 10, 15, and 20. At time $t=0$ we notice a stronger excitation of high momentum components in the negative k_z direction as com-

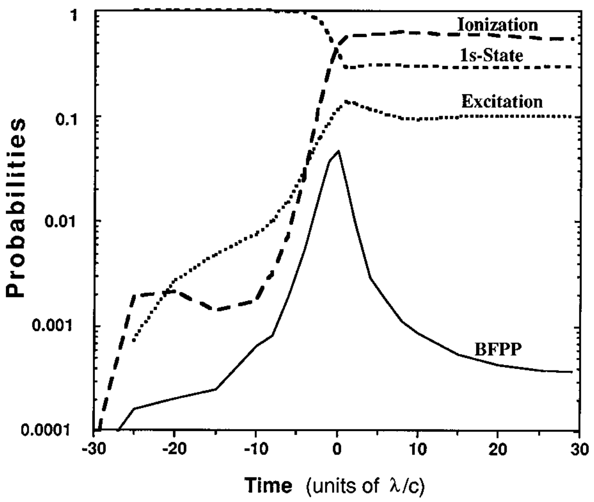

FIG. 8. Time evolution of the occupation probabilities for the collision system shown in Fig. 6 obtained by projection on the various sets of target states. The corrections with respect to the overlap of the projectile states with the target states have not been included here, since *K*-shell transfer amounts only to 2.5%.

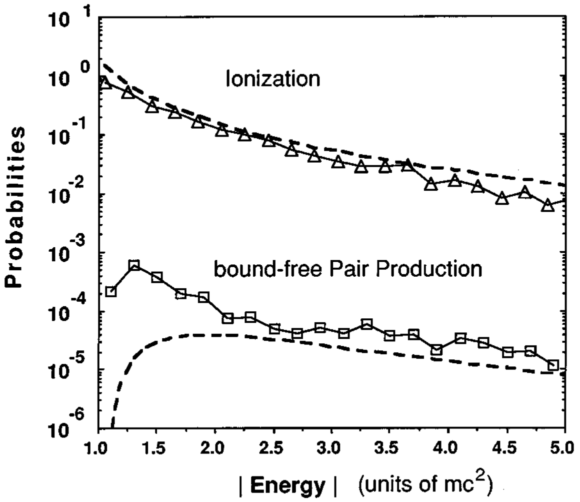

FIG. 9. Results of the projections of the time evolved state taken at time $t = 20$ onto the positive and negative continuum as a function of the absolute value of the energy. The dashed lines show the corresponding perturbation theory results for ionization and bound-free pair production.

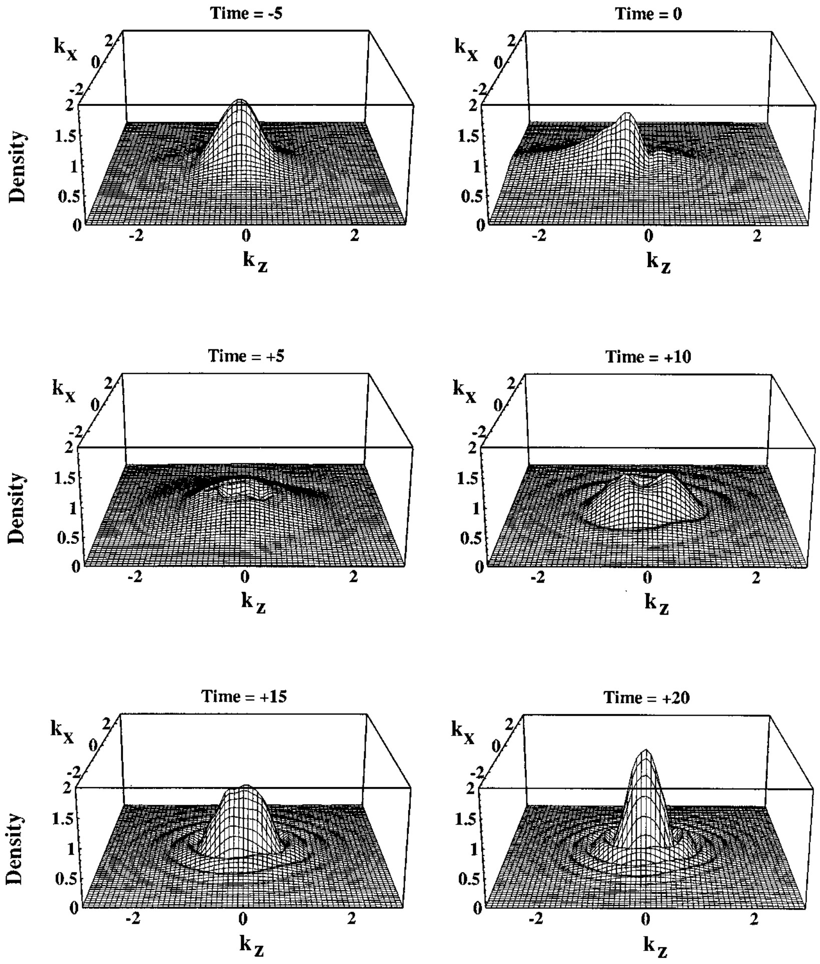

FIG. 10. Time evolution of the momentum space density in the collision system Au + U at $E_{\mathrm{lab}} = 10$ GeV/nucleon and impact parameter zero.

pared to the results at $\gamma=2$. Around $k_z=0$ the momentum space density looks as if it is being "pinched" by the Lorentz-contracted field of the projectile. At larger positive times, the wave function appears to be *less* perturbed as compared to Fig. 6, especially since we observe fewer high momentum components going in the forward direction. Correspondingly, we found the probability for ionization going down from 54% at $\gamma=2$ to 30.4% at $\gamma=11.7$, whereas it has been predicted by perturbation theory to saturate to a value of about 51% above $\gamma=2$ [46]. Running the 3D version of the MasPar code, we find that the suppression of the ionization becomes less pronounced with increasing impact parameter. In particular, our results merge into perturbation theory for impact parameters larger than 2λ.

The probability for inner-shell excitation has been found to be remarkably γ independent and amounts to about 12.8%.

For bound-free pair production we find a value of 3.3×10^{-4}. The energy integration has been extended up to $|E|=10$ and the angular momentum summation up to $|\kappa|=10$. This value for the *total* probability agrees within our accuracy with the perturbation theory prediction of 4×10^{-4}. However, it has to be pointed out that it would be deceiving to speak of "agreement with perturbation theory," since the energy and angular momentum distributions obtained in both calculations are quite different in detail. This result is important, as it indicates that we cannot confirm any "nonperturbative enhancement" for bound-free pair production at this collision energy. In contrast, an enhancement by 1–2 orders of magnitude has been reported previously for a comparable collision system, using the finite-differences method [15].

3. Impact parameter study and total cross sections

Next, we give an example of a collision at a large impact parameter that has been run on the MasPar using the 3D grid with $(12\times24\times14)$ points in cylindrical coordinates ($k_\perp$, k_z, and ϕ_k) for the system Au+U at 0.93 GeV/nucleon. In Fig. 11 we display the momentum space density in a collision with an impact parameter of 4λ at time $t=20$ in comparison to a collision at zero impact parameter. This figure demonstrates that the wave function gets distorted by a transversal momentum transfer, but the perturbation is in general much weaker than at zero impact parameter. For example, the ionization probability goes down from 54% at impact parameter 0 to 6.55% at impact parameter 4.

Since the grid dimensions in this calculation are determined by the MasPar machine size, we have not performed a systematic convergence check for the 3D calculation yet. Judging from a comparison of the 3D results obtained with the MasPar to those obtained with PVM on an even "coarser" grid, the MasPar results for the dominant processes, namely, ionization and excitation, appear to be converged within an accuracy of a few percent. Therefore, we are able to present impact parameter dependences and total cross sections for ionization and excitation, The impact parameter dependences of the probabilities for the initial 1s state, excitation, and ionization are shown in Fig. 12. The impact parameter ranges from 0 to 4. Ionization has a global maximum at zero impact parameter and drops continuously with growing impact parameters, while excitation has its global maximum around 0.5λ (193 fm). The excitation probabilities up to the $3p_{1/2}$ state are shown in Fig. 13. Both the excitation probabilities for the $2s_{1/2}$ and the $3s_{1/2}$ have their global maxima around 0.5λ, while the probabilities of the p states extend over a large impact parameter range.

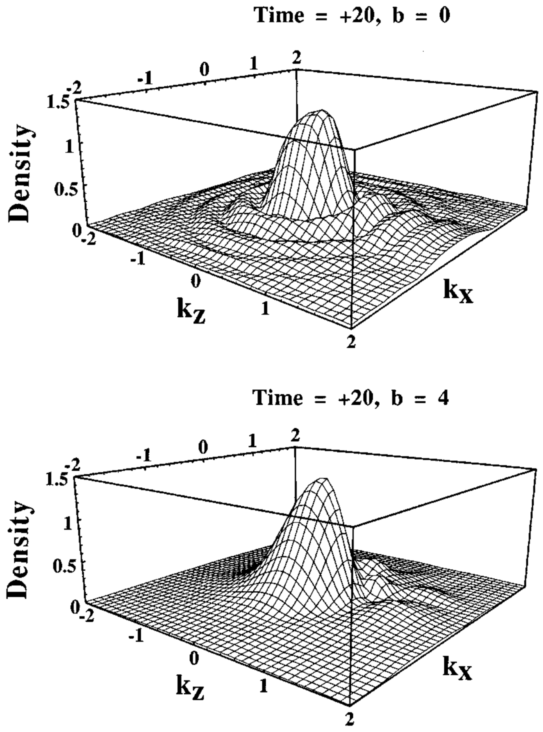

FIG. 11. Comparison of the momentum space density at two different impact parameters b, namely, (a) $b=0$ and (b) $b=4\lambda$. The collision system is Au + U at 0.93 GeV/nucleon, the time is $t=+20$. The zero impact parameter has been run with a 2D grid of (32×128) in ρ and z and the impact parameter $b=4$ has been run with a grid of $(12\times24\times14)$ points in (ρ,z,ϕ).

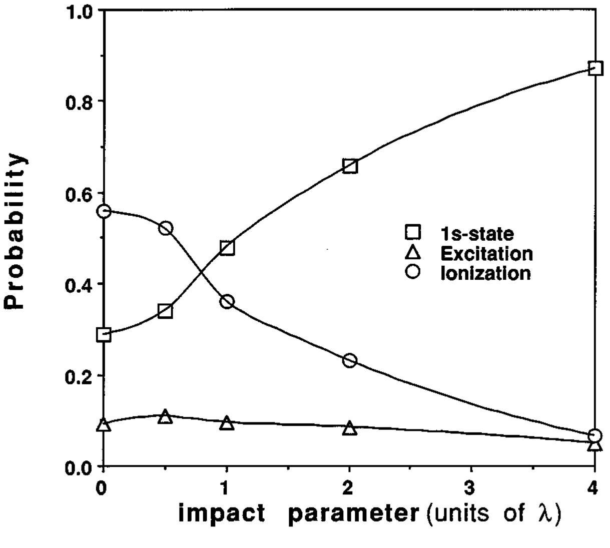

FIG. 12. Impact parameter dependences for the 1s state, total excitation, and ionization for the collision system Au + U at 0.93 GeV/nucleon.

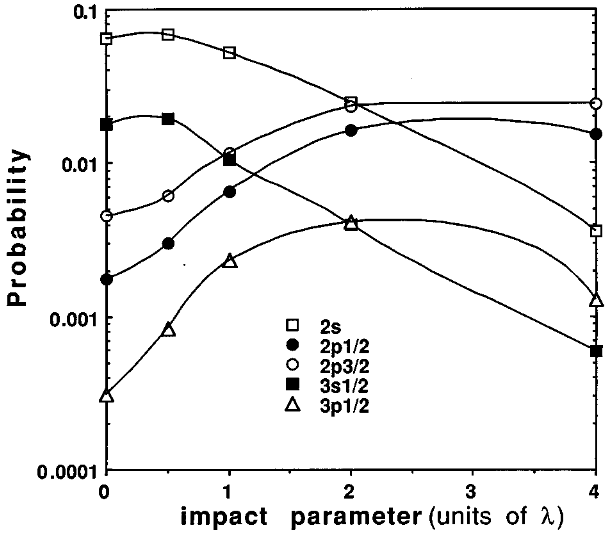

FIG. 13. Impact parameter dependences for various inner-shell states ranging from the $2s_{1/2}$ up to the $3p_{1/2}$ state for the collision system Au + U at 0.93 GeV/nucleon.

From the curves in Fig. 12 total excitation and ionization probabilities have been calculated. To estimate the contribution from impact parameter $b=4\lambda$ to ∞ an exponential extrapolation has been employed. We obtained an ionization cross section of 14.4 kb, which practically agrees with the value in perturbation theory of 14.7 kb. For excitation, the total cross section amounts to 8.26 kb. The $2s_{1/2}$ and $3s_{1/2}$ states contribute to the excitation cross section with 1.37 and 0.25 kb, respectively.

For the case of bound-free pair production, we encountered the problem that the probabilities as a function of impact parameter do not drop below a value of the order of 10^{-4}. The "coarse" grid on the MasPar does not provide sufficient accuracy to describe probabilities below 10^{-4}. At the present stage we can only give a crude estimate of the total cross section by assuming a constant, impact parameter independent background, which we subtract for all impact parameters. Doing so, we obtained probabilities for bound-free pair production, which drop reasonably fast on the impact parameter range from 0 to 2λ. For larger impact parameters we extrapolated with the perturbation theory results. With this procedure, we obtain a cross section of 2.33 b, which overshoots the cross section in perturbation theory of 0.96 b by only a factor of 2.4 and furthermore agrees well with the experimental cross section of 2.2 b (the latter including capture to all bound states, which typically account for about 20% of the total cross section). We admit that the assumptions to extract this cross section are rather crude and we regard the agreement as accidental. Future work with a refined 3D grid will be necessary to predict cross sections for bound-free pair production reliably.

4. Remarks on convergence and accuracy

To get an estimate of the convergence of our calculation, we compared results at zero impact parameter obtained with the grid used for PVM ($13\times7\times10$ points) and the "coarse" grid used for the 3D calculation on the MasPar ($12\times24\times14$ points) with the 2D grid on the MasPar (32×128 points). Again, we are considering the system Au + U at 0.93 GeV/nucleon. It turned out that further refinement of the grid yields values for bound-free pair production that are closer to the perturbation theory result, while ionization remains basically unaffected. For example, the result obtained with PVM on the coarser grid explained above yields a final probability for bound-free pair production of about 10^{-3} for this collision system; i.e., the refinement of the grid on the MasPar reduced the probability by a factor of 2. A further refinement has not been performed yet.

The normalization of the time evolved wave function has been found to be remarkably stable, although we do not enforce normalization by any means. For example, in the collision system considered here, we find a norm of 0.999 30 at time $t=-25$ and 0.9955 at $t=+10$. Beyond +20, however, the normalization dropped to reach a value of about 94% at $t=+30$. The projections for bound-free pair production, excitation, and the 1s state remained practically unaffected by this loss of normalization, whereas the projection onto the positive continuum decreased. This indicates that the loss of normalization is due to positive continuum waves that have reached the boundaries of the volume at larger times and that these waves are not reflected completely.

A further test of our accuracy is the summation of our projections on the complete set of target states. In case of the collision system at $\gamma=2$, we typically arrive at 98% of the total norm or better, if we extend the projections to energies as high as $|E|=8$ in both continua.

IV. SUMMARY

The one-electron Dirac equation that governs the electron behavior in relativistic heavy-ion collisions has been transformed to momentum space, where it has the form of a time-dependent integral equation. By discretization on a grid in momentum space, this integral equation goes over into a system of coupled differential equations. The wave function is represented on the grid by a global 3D interpolation function, which is constructed from a 2D spline function and a quadratic interpolation. The time propagation is performed with a standard predictor-corrector routine. The right-hand side of this system of differential equations is given by a numerical integral over momentum space. Probabilities can be extracted for inner-shell ionization, excitation, transfer to the projectile, and bound-free pair production. Calculations have been performed in the energy range from $E_{\mathrm{lab}}=0.24$ to 10 GeV/nucleon. At 0.24 GeV/nucleon we have shown that our formalism implements a closed-form description of the charge transfer as well as the ionization process. We found that the transfer process is rapidly going down with increasing collision energy. At higher collision energies, we concentrated on ionization and bound-free pair production. Bound-free pair production has been predicted by previous coupled-channel calculations to exceed the results of perturbation theory of first order by typically more than one order of magnitude in this collision energy range. At a collision energy of 0.93 GeV/nucleon and impact parameter zero we found an enhancement of merely about a factor of 4–5 compared to perturbation theory. This enhancement effect has been found to go down with increasing collision energy. We conclude that the previously published coupled-channel calculations overestimate bound-free pair production due to the truncation of the atomic basis set being used.

The ionization rate has been found to decrease with increasing collision energy. This is an astounding result, since it disagrees with perturbation theory, but also with the prediction by Baltz, Rhoades-Brown, and Weneser [17,18], who claim that *all* processes are going to become γ independent. Therefore, the energy dependence of the ionization process will be subject to future investigations at much higher collision energies.

As a further visualization of the scattering process, we computed the electron density in configuration space using FFT. This gave us useful information on the angular distribution of the ionization process and clearly demonstrated the inclusion of the transfer channel in our formalism.

Most of the results in this paper have been presented at zero impact parameter, which allowed reduction of the calculation to two dimensions. For a reasonably accurate 3D calculation a further refinement of the grid will be necessary.

ACKNOWLEDGMENTS

We thank Dr. Harvey Gould for fruitful discussions and his continuing interest. We thank the Information and Computing Sciences Division at LBL for its support and in particular we thank Ruth Hinkins for introducing us to parallel computing. We thank Jim Feagin for introducing us to MATHEMATICA. One of us (A.H.S.) thanks the Chemical Sciences Division of LBL for the friendly hospitality during his stay at LBL. This work was supported by the Director, Office of Energy Research, Office of Basic Energy Sciences, Division of Chemical Sciences, of the U.S. Department of Energy (DOE) under Contract No. DE-AC-03-76SF00098 and by the Danish Natural Science Research Council. One of us (K.M.) was partially supported by DAAD (Deutscher Akademischer Austauschdienst).

APPENDIX: ATOMIC WAVE FUNCTIONS IN MOMENTUM SPACE

Our method for computing the atomic wave functions in momentum space is based on the work by Sørensen and Belkacem [55]. We are going to review some of their equations, and discuss some important properties of the continuum wave functions and the differences in our numerical technique compared to theirs. In addition to [55], we derive expressions for bound projectile states that are needed for the description of the electron transfer.

1. The Dirac spinor in momentum space

The standard representation of the relativistic Dirac spinor in a spherical symmetric field is [68]

$$\phi(\vec{r})=\begin{pmatrix}\phi^{u}(\vec{r})\\ \phi^{l}(\vec{r})\end{pmatrix}=\begin{pmatrix}g(r)\chi_{\kappa}^{\mu}(\theta,\phi)\\ if(r)\chi_{-\kappa}^{\mu}(\theta,\phi)\end{pmatrix}. \tag{A1}$$

Here, $g(r)$ and $f(r)$ are the radial components of the upper and lower components, respectively. The $\chi_{\kappa}^{\mu}(\theta,\phi)$ are the spin-angular functions with good angular momentum j and μ_j:

$$\chi_{\kappa}^{\mu}=\sum_{m=\pm 1/2}\langle l,\mu-m,1/2,m|j,\mu\rangle Y_l^{\mu-m}(\theta,\phi)\xi_m, \tag{A2}$$

where $\langle\ \rangle$ denotes a Clebsh-Gordan coefficient, Y_l^m a spherical harmonic, and ξ_m a Pauli spin eigenfunction. The transformation to momentum space is performed according to Eq. (2.9). Using the series expansion of the exponential [60]

$$e^{i\vec{k}\cdot\vec{r}}=4\pi\sum_{l=0}^{\infty}\sum_{m=-l}^{l} i^l j_l(kr)Y_l^{m*}(\theta_k,\phi_k)Y_l^m(\theta,\phi) \tag{A3}$$

we arrive at the following representation for the Dirac spinor in momentum space [69]:

$$\tilde{\phi}(\vec{k})=i^{-l}\begin{pmatrix}g(k) & \chi_{\kappa}^{\mu} & (\theta_k,\phi_k)\\ -\mathrm{sgn}(\kappa)f(k) & \chi_{-\kappa}^{\mu} & (\theta_k,\phi_k)\end{pmatrix}. \tag{A4}$$

The radial integrals are defined as

$$\begin{aligned}\tilde{g}(k)&=(2/\pi)^{1/2}\int_0^{\infty}g(r)j_l(kr)r^2dr,\\ \tilde{f}(k)&=(2/\pi)^{1/2}\int_0^{\infty}f(r)j_{\bar{l}}(kr)r^2dr,\end{aligned} \tag{A5}$$

where $\bar{l}$ is the orbital momentum quantum number related to $-\kappa$: $\bar{l}=l-\mathrm{sgn}(\kappa)$ and j_l are the spherical Bessel functions. The evaluation of these integrals is shown in the next sections.

2. Radial integrals for momentum space wave functions

a. Continuum wave functions

The radial functions $g(r)$ and $f(r)$ with a given energy E and angular momentum κ in *configuration* space are

$E>1$:

$$\left.\begin{matrix}g_{\kappa}(r)\\ f_{\kappa}(r)\end{matrix}\right\}=Nr^{s-1}\times\left\{\begin{matrix}(E+1)^{1/2}\mathrm{Re}\\ -(E-1)^{1/2}\mathrm{Im}\end{matrix}\right\}\times[e^{-ik_0r}e^{i\delta}(s+i\eta)_1F_1(1+s+i\eta,2s+1,2ik_0r)]. \tag{A6}$$

For $E<-1$ the factors in braces have to be replaced by $(|E|-1)^{1/2}$ and $+(|E|+1)^{1/2}$. The parameters are

$$s=[\kappa^2-(Z_Te^2)^2]^{1/2},\quad k_0=(E^2-1)^{1/2},\quad \eta=Z_Te^2E/k_0,$$

$$e^{2i\delta}=(-\kappa+i\eta/E)/(s+i\eta), \tag{A7}$$

$$N=\frac{e^{\pi\eta/2}|\Gamma(s+i\eta)|2^sk_0^{s-1/2}}{\pi^{1/2}\Gamma(2s+1)}.$$

We have to solve the following radial integral:

$$I_{\kappa}=\int_0^{\infty}j_l(kr)r^{s+1}e^{-ik_0r}{}_1F_1(s+1+i\eta,2s+1,i2k_0r)dr. \tag{A8}$$

Now we make use of a series expansion of the spherical Bessel functions [64,70]:

$$j_l(z)=\frac{1}{2z}\sum_{n=0}^{l}\frac{(l+n)!}{n!(l-n)!}\frac{1}{(2z)^n}\left(i^{n-l-1}e^{iz}+i^{l+1-n}e^{-iz}\right). \tag{A9}$$

This leads to the following expression for the radial integral I_κ:

$$I_\kappa(k)=\frac{1}{2k}\sum_{n=0}^{l}\frac{(l+n)!}{n!(l-n)!}\frac{1}{(2k)^n}[i^{n-l-1}I_A(k)+i^{l+1-n}I_B(k)]. \tag{A10}$$

The integrals $I_A(k)$ and $I_B(k)$ are given by

$$I_A(k)=\int_0^\infty e^{-i(k_0-k)r}r^{s-n}{}_1F_1(s+1+i\eta,2s+1,i2k_0r)dr,$$

$$I_B(k)=\int_0^\infty e^{-i(k_0+k)r}r^{s-n}{}_1F_1(s+1+i\eta,2s+1,i2k_0r)dr. \tag{A11}$$

Now we apply Kummer's transformation [64,68]:

$$e^{-ik_0r}{}_1F_1(1+s+i\eta,2s+1,2ik_0r)=e^{ik_0r}{}_1F_1(s-i\eta,2s+1,-2ik_0r) \tag{A12}$$

to I_A to obtain

$$I_A(k)=\left[\int_0^\infty e^{-i(k_0+k)r}r^{s-n}{}_1F_1(s+i\eta,2s+1,i2k_0r)dr\right]^*, \tag{A13}$$

where the $*$ stands for "complex conjugate." With the following integral representation of the hypergeometric ${}_2F_1$ functions [71,72],

$$\int_0^\infty dx x^\mu e^{-\nu x}{}_1F_1(a,b,cx)=\Gamma(\mu+1)\nu^{-(\mu+1)}{}_2F_1(\mu+1,a,b,c/\nu), \tag{A14}$$

we finally find the expressions

$$I_A(k)=\Gamma(s-n+1)\left[[i(k_0+k)]^{-(s-n+1)}\times{}_2F_1\left(s-n+1,s+i\eta,2s+1,\frac{2k_0}{k_0+k}\right)\right]^*,$$

$$I_B(k)=\Gamma(s-n+1)[i(k_0+k)]^{-(s-n+1)}\times{}_2F_1\left(s-n+1,s+1+i\eta,2s+1,\frac{2k_0}{k_0+k}\right). \tag{A15}$$

Depending on the parameter values of the ${}_2F_1$ functions, a singularity may occur at the argument value $x=2k_0/(k_0+k)=1$. We defined a small area around the singular point with a radius of typically 0.2. Outside this area, the ${}_2F_1$ functions could be evaluated with the Gaussian series expansions and its analytical continuations [see, e.g., Eqs. (15.1.1), (15.3.3)–(15.3.9) in [64] or Eqs. (9.100), (9.131), and (9.132) in [71]]. To obtain the values in the vicinity of the singularity $x=1$ with sufficiently high precision, we solve the hypergeometric differential equation [(15.5.1) in [64]] by direct numerical integration using the predictor-corrector code DE by Shampine and Gordon [73]. Therefore, the hypergeometric differential equation had to be rewritten as a first-order equation, using the differentiation formula of the Gaussian series [(15.2.1) in [64]] for the starting values of the first derivative. The initial values were taken from the series expansions outside the area around the singularity. With this procedure, we could integrate as close as 10^{-10} towards the singularity at $x=1$. The properties of the radial wave functions shall not be reviewed here; they are fully explained in [55]. In this paper, the authors evaluated the ${}_2F_1$ functions by direct numerical evaluation of the contour-integral representation (15.3.1) in [64] using a Simpson-quadrature formula. Therefore, they had to introduce a "convergence factor" $\exp(-\epsilon k_0 r)$ in the integrand of Eq. (A11) to make the quadrature feasible. Note that it was not yet necessary for us to introduce this convergence factor. The expressions in Eq. (A15) can be evaluated as they are. However, to make the numerical projection of the final state on these continuum functions possible (i.e., to compute the overlap), it turned out that we have to adopt the same technique. The reason lies in the peculiarities of the continuum functions in momentum space. They exhibit a singularity at $k/k_0=1$. In the vicinity of this singular point the radial wave functions are having an infinite number of oscillations, while they are smooth outside this area. The convergence factor $\exp(-\epsilon k_0 r)$ smoothens these wild oscillations and gives the radial density of the continuum wave functions a certain ϵ-dependent width. To account for the convergence factor $\exp(-\epsilon k_0 r)$ in Eq. (A15), only the denominator k_0+k of the argument x has to be modified to $[k_0(1-i\epsilon)+k]$. ϵ is usually set to 10^{-3}. We checked that the actual value of ϵ does not essentially affect the values of the projections if it is chosen to be in the range from 10^{-2} to 10^{-4}. The projection is performed with a 3D Gauss-Legendre quadrature formula in spherical coordinates. To account for the singularity at $k/k_0=1$, the area around this point has to be integrated with very high accuracy.

b. Bound-state wave functions

The radial bound-state functions are given by [70]

$$g_{n,\kappa}(r)=Ne^{-\beta r}r^{s-1}\sum_{m=0}^{n'}c_{i,m}^{+}r^m,$$

$$f_{n,\kappa}(r)=Ne^{-\beta r}r^{s-1}\sum_{m=0}^{n'}c_{i,m}^{-}r^m, \tag{A16}$$

with

$$N=\frac{\beta^{s+1/2}2^{s}}{\Gamma(2s+1)}\left(\frac{\Gamma(2s+n'+1)}{2n'!K(K-\kappa)}\right)^{1/2}$$

$$c^{\pm}_{i,m}=(1\pm E)^{1/2}2^{m}\left(\frac{(-n')_m[m-n'\pm(K-\kappa)]}{m!(2s+1)_m}\right)\beta^{m} \tag{A17}$$

and

$$s=[\kappa^2-(Z_Te^2)^2]^{1/2},\quad n'=n-|\kappa|, \tag{A18}$$

$$K=[n^2-2n'(|\kappa|-s)]^{1/2},$$

$$\beta=\frac{Z_Te^2}{K},\quad E=\left[1+\left(\frac{Z_Te^2}{n'+s}\right)^2\right]^{-1/2}.$$

The spherical Bessel functions are related to the Bessel functions of fractional order by [60]

$$j_l(x)=\sqrt{\frac{\pi}{2x}}J_{l+1/2}(x). \tag{A19}$$

According to [71], we have

$$\int_0^{\infty}e^{-\alpha x}J_{\nu}(\beta x)x^{\mu-1}dx=\frac{(\beta/2)^{\nu}\Gamma(\nu+\mu)}{(\alpha^2+\beta^2)^{(\nu+\mu)/2}\Gamma(\nu+1)}\ {}_2F_1\left(\frac{\nu+\mu}{2},\frac{1-\mu+\nu}{2},\nu+1,\frac{\beta^2}{\alpha^2+\beta^2}\right). \tag{A20}$$

Putting it all together, we find

$$\tilde{g}_{n,\kappa}(k)=\frac{N}{\sqrt{k}}\sum_{m=0}^{n'}c^{+}_{i,m}I_{m,l},$$

$$\tilde{f}_{n,\kappa}(k)=\frac{N}{\sqrt{k}}\sum_{m=0}^{n'}c^{-}_{i,m}I_{m,\bar{l}}, \tag{A21}$$

where

$$I_{m,l}=\frac{(k/2)^{l+1/2}\Gamma(s+m+l+2)}{(\beta^2+k^2)^{(s+m+l+2)/2}\Gamma(l+3/2)}\ {}_2F_1\left(\frac{s+m+l+2}{2},\frac{l-s-m}{2},l+\frac{3}{2},\frac{k^2}{k^2+\beta^2}\right). \tag{A22}$$

For the evaluation of these expressions we are basically using the same computer code as for the continuum wave functions. The bound states are much simpler to evaluate though, since we need to cover only the argument range from 0 to 1 for the ${}_2F_1$ functions and they have only a finite number of nodes. Therefore, also the "convergence factor" can be omitted. The important feature of the radial bound-state wave functions in momentum space is that they are regular at the origin, while their counterparts in configuration space exhibit the well-known singularity proportional to r^{s-1}.

3. Projectile wave functions

An electron in an eigenstate ϕ_j of the projectile is described in configuration space coordinates of the target as [see Eqs. (2.18) and (5.2) in [23]]

$$\phi_{P,j}(\vec{r},t)=S^{-1}\phi_j(\vec{r}\,')e^{-iE_jt'}. \tag{A23}$$

The relation between the target frame coordinates $(\vec{r},t)$ and the projectile frame coordinates $(\vec{r}\,',t')$ is given by the Lorentz transformation

$$(\vec{r},t)=(x,y,z,t),$$

$$(\vec{r}\,',t')=(x-b,y,\gamma(z-v_Pt),\gamma(t-v_Pz)), \tag{A24}$$

and S is the Lorentz-boost operator [74]

$$S^{-1}=\left(\frac{\gamma+1}{2}\right)^{1/2}(1+\delta\alpha_z),\quad \delta=\left[\frac{\gamma-1}{\gamma+1}\right]^{1/2}. \tag{A25}$$

The Fourier transform $\tilde{\phi}_j(\vec{k}\,')$ of $\phi_j(\vec{r}\,')$ in momentum space coordinates of the *projectile-frame* $\vec{k}\,'$ is

$$\tilde{\phi}_j(\vec{k}\,')=\frac{1}{(2\pi)^{3/2}}\int d^3r'\,e^{-i\vec{k}'\cdot\vec{r}'}\phi_j(\vec{r}\,'). \tag{A26}$$

Now we define the Fourier transform of $\phi_{P,j}(\vec{r})$ in *target-frame* momentum space coordinates:

$$\begin{aligned}\tilde{\phi}_{P,j}(\vec{k},t)&=\frac{1}{(2\pi)^{3/2}}\int d^3r e^{-i\vec{k}\cdot\vec{r}}\phi_{P,j}(\vec{r},t)\\&=\frac{1}{(2\pi)^{3/2}}\int d^3rS^{-1}\phi_j(\vec{r}\,')e^{-iE_jt'}e^{-i\vec{k}\cdot\vec{r}}\\&=\frac{1}{(2\pi)^{3}}\int\int d^3rd^3k'S^{-1}\tilde{\phi}_j(\vec{k}\,')\\&\quad\times e^{i\vec{k}'\cdot\vec{r}'-i\vec{k}\cdot\vec{r}}e^{-iE_jt'}.\end{aligned} \tag{A27}$$

With $x'=x-b$ and $y'=y$ we can perform the integral over x and y and obtain with the substitution $\gamma k'_z=\zeta$,

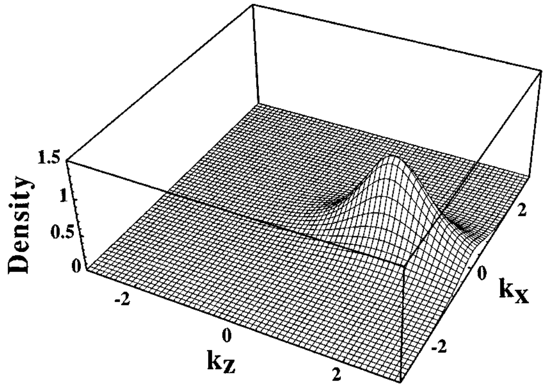

FIG. 14. Momentum space density of the 1*s* state of the Au projectile at $E_{\text{lab}}=0.93$ GeV/nucleon, time $t=+10$ and impact parameter zero. The density has a maximum at $k_z=0.76$ and is stretched along the k_z axis by the value of $\gamma=2$.

$$\frac{1}{2\pi\gamma}\int\int dz d\zeta S^{-1}\tilde{\phi}_j(k_x,k_y,\zeta/\gamma) \times e^{i[(\zeta-k_z+\gamma E_j v_p)z-k_x b-(\zeta v_P+\gamma E_j)t]}. \tag{A28}$$

The z integration yields

$$\frac{S^{-1}}{\gamma}\tilde{\phi}_j\left(k_x,k_y,\frac{k_z}{\gamma}-v_P E_j\right)e^{i[(-\zeta v_P-\gamma E_j)t-k_x b]}, \tag{A29}$$

with $\zeta=k_z-\gamma v_P E_j$. Finally, we arrive at

$$\tilde{\phi}_{P,j}(\vec{k},t)=\frac{S^{-1}}{\gamma}\tilde{\phi}_j\left(k_x,k_y,\frac{k_z}{\gamma}-v_P E_j\right)e^{-i[(k_z v_P+E_j/\gamma)t+k_x b]}. \tag{A30}$$

The projectile states are shifted forward by the momentum $\gamma v_P E_j$ and "stretched" by the factor γ. The numerical evaluation can be done basically with the same methods as in the case of the target states that we explained in the previous sections.

We want to illustrate with a typical example that a projectile bound state predominantly overlaps with the positive continuum of the target, while the overlap with the negative continuum is small, but not necessarily negligible. The collision system is gold on uranium at $E_{\text{lab}}=$ 0.93 GeV/nucleon ($\gamma=2$). We have set the impact parameter to zero, which helps to speed up the computation considerably since we only have to integrate numerically over the k_x-k_z plane. In Fig. 14 we plotted the density of the projectile 1*s* state in a window of the k_x-k_z plane ranging from -3 to 3 in both coordinates. The time has been set to $t=10$. The projectile is traveling in coordinate space along the z axis, meaning that the momentum of the projectile is pointing into the positive k_z direction. We find the maximum of the wave function around $k_z=\gamma E_{1s}v_P=1.415$ [see Eq. (A30)]. It is also obvious in this picture that the projectile wave function is stretched in k_z direction by the Lorentz factor γ. In the next step we projected this wave function by projection onto the target wave functions out of the positive and negative continua. For the projection, the analytical representation of both states has been used and not their grid representation. The angular momentum summation has been extended up to $|\kappa|=10$. In Fig. 15 we display the projection of the projectile 1*s* state onto the positive and negative continua of the target. The energy integration yields a value of 81.9% for the positive continuum and 1.8% for the negative continuum. The projection onto the bound states of the target up to the M shell was found to be less than 1×10^{-3}. About 16% are missing due to the restriction of the angular momenta in the continuum states to $|\kappa|\leqslant10$. The maximum of the projection on the positive continuum is found around $E=1.7$, which corresponds to a momentum of $k_z=\sqrt{E^2-1}=1.375$ and agrees very well with the maximum found in Fig. 14.

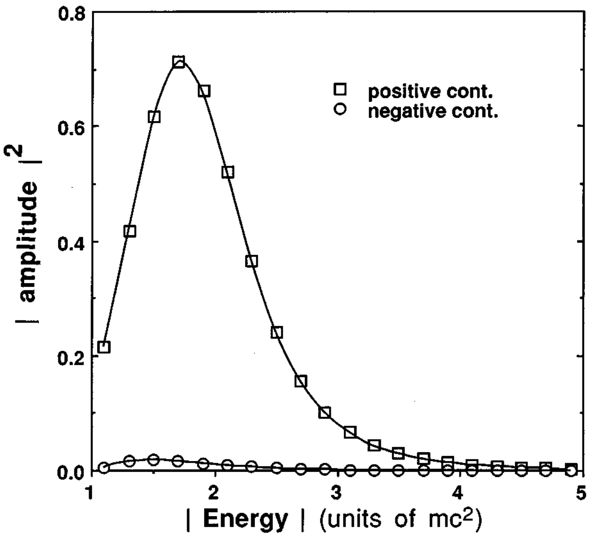

FIG. 15. Projections of the 1*s* state of a Au projectile at $E_{\text{lab}}=0.93$ GeV/nucleon and time $t=+10$ onto the positive and negative continuum states of the target. The projections are shown as a function of the continuum energy.

---

[1] R. Anholt, W. E. Meyerhof, Ch. Stoller, E. Morenzoni, S. A. Adriamonje, J. D. Molitoris, O. K. Baker, D. H. H. Hoffmann, H. Bowman, J.-S. Xu, Z.-Z. Xu, K. Frankel, D. Murphy, K. Crowe, and J. O. Rasmussen, Phys. Rev. A **30**, 2234 (1984).
[2] R. Anholt, W. E. Meyerhof, H. Gould, Ch. Munger, J. Alonso, P. Thieberger, and H. E. Wegener, Phys. Rev. A **32**, 3302 (1985).
[3] R. Anholt, W. E. Meyerhof, X.-Y. Xu, H. Gould, B. Feinberg, R. J. McDonald, H. E. Wegener, and P. Thieberger, Phys. Rev. A **36**, 1586 (1987).
[4] W. E. Meyerhof, R. Anholt, J. Eichler, H. Gould, Ch. Munger, J. Alonso, P. Thieberger, and H. E. Wegener, Phys. Rev. A **32**, 3291 (1985).
[5] W. E. Meyerhof, R. Anholt, X.-Y. Xu, H. Gould, B. Feinberg,

R. J. McDonald, H. E. Wegner, and P. Thieberger, Phys. Rev. A **35**, 1967 (1987).

[6] H. Berg, R. Dörner, C. Kelbch, S. Kelbch, J. Ullrich, S. Hagmann, P. Richard, H. Schmidt-Böcking, A. S. Schlachter, M. Prior, H. J. Crawford, J. M. Engelage, I. Flores, D. H. Loyd, J. Pedersen, and R. E. Olson, J. Phys. B **21**, 3929 (1988).

[7] H. Berg, O. Jagutzki, R. Dörner, R. D. DuBois, C. Kelbch, H. Schmidt-Böcking, J. A. Tanis, A. S. Schlachter, L. Blumenfeld, B. d'Etat, S. Hagmann, A. Gonzales, and T. Quinteros, Phys. Rev. A **46**, 5539 (1992).

[8] A. Belkacem, H. Gould, B. Feinberg, R. Bossingham, and W. E. Meyerhof, Phys. Rev. Lett. **71**, 1514 (1993).

[9] A. Belkacem, H. Gould, B. Feinberg, R. Bossingham, and W. E. Meyerhof, Phys. Rev. Lett. **73**, 2432 (1994).

[10] H. Gould, Lawrence Berkeley Laboratory Report No. LBL-18593, 1984 (unpublished).

[11] U. Becker, N. Grün, and W. Scheid, J. Phys. B **20**, 2075 (1987).

[12] K. Rumrich, K. Momberger, G. Soff, W. Greiner, N. Grün, and W. Scheid, Phys. Rev. Lett. **66**, 2613 (1991).

[13] M. Fatyga, M. J. Rhoades-Brown, M. J. Tannenbaum (unpublished).

[14] K. Momberger, N. Grün, and W. Scheid, Z. Phys. D **18**, 133 (1991).

[15] J. Thiel, A. Bunker, K. Momberger, N. Grün, and W. Scheid, Phys. Rev. A **46**, 2607 (1992).

[16] K. Momberger, J. Thiel, Th. Lippert, N. Grün, and W. Scheid, in *Proceedings of the Predeal International Summer School: New Trends in Theoretical and Experimental Nuclear Physics, Predeal, Romania, 1991*, edited by A. A. Raduta, D. S. Delion, and I. I. Ursu (World Scientific, Singapore, 1992), pp. 484–506.

[17] A. J. Baltz, M. J. Rhoades-Brown, and J. Weneser, Phys. Rev. A **44**, 5569 (1991).

[18] A. J. Baltz, M. J. Rhoades-Brown, and J. Weneser, Phys. Rev. A **47**, 3444 (1993).

[19] M. J. Rhoades-Brown, C. Bottcher, and M. R. Strayer, Phys. Rev. A **40**, 2831 (1989).

[20] A. Westphal and Y. D. He, Phys. Rev. Lett. **71**, 1160 (1993).

[21] C. R. Vane, S. Datz, P. F. Dittner, H. F. Krause, C. Bottcher, M. Strayer, R. Schuch, H. Gau, and R. Hutton, Phys. Rev. Lett. **69**, 1911 (1992).

[22] C. A. Bertulani and G. Baur, Phys. Rep. **163**, 299 (1988).

[23] J. Eichler, Phys. Rep. **193**, 167 (1990).

[24] J. Eichler and W. E. Meyerhof, *Relativistic Atomic Collisions* (North-Holland, Amsterdam, 1995).

[25] P. A. Amundsen and K. Aashamar, J. Phys. B **14**, 4047 (1981).

[26] G. R. Deco and R. D. Rivarola, J. Phys. B **21**, L299 (1988); **21**, 1861 (1988); **21**, 1229 (1988); **22**, 1043 (1989).

[27] G. R. Deco and N. Grün, J. Phys. B **22**, 1357 (1989); **22**, 3709 (1989).

[28] G. Deco, K. Momberger, and N. Grün, J. Phys. B **23**, 2091 (1990).

[29] R. Anholt, Phys. Rev. A **19**, 1004 (1979).

[30] U. Becker, J. Phys. B **20**, 6563 (1987).

[31] F. Decker, Phys. Rev. A **44**, 2883 (1991).

[32] D. C. Ionescu and J. Eichler, Phys. Rev. A **48**, 1176 (1993).

[33] U. Becker, N. Grün, and W. Scheid, J. Phys. B **18**, 4589 (1985).

[34] U. Becker, N. Grün, and W. Scheid, J. Phys. B **19**, 1347 (1986).

[35] K. Momberger, N. Grün, W. Scheid, and U. Becker, J. Phys. B **22**, 3269 (1989).

[36] A. J. Baltz, M. J. Rhoades-Brown, and J. Weneser, Phys. Rev. A **48**, 2002 (1993).

[37] U. Becker, N. Grün, W. Scheid, and G. Soff, Phys. Rev. Lett. **56**, 2016 (1986).

[38] K. Momberger, N. Grün, W. Scheid, and U. Becker, J. Phys. B **23**, 2293S (1990).

[39] K. Momberger, N. Grün, and W. Scheid, J. Phys. B **26**, 1851 (1993).

[40] C. Best, W. Greiner, and G. Soff, Phys. Rev. A **46**, 261 (1992).

[41] D. C. Ionescu, Phys. Rev. A **49**, 3188 (1994).

[42] Th. de Reus, U. Müller-Nehler, G. Soff, J. Reinhardt, S. Graf, B. Müller, and W. Greiner, Phys. Rev. C **40**, 752 (1989).

[43] N. Toshima and J. Eichler, Phys. Rev. Lett. **60**, 573 (1988).

[44] N. Toshima and J. Eichler, Phys. Rev. A **38**, 2305 (1988).

[45] N. Toshima and J. Eichler, Phys. Rev. A **40**, 125 (1989).

[46] U. Becker, Ph.D. thesis, Giessen, 1986; see *Physics of Strong Fields*, Vol. 153 of *NATO Advanced Study Institute Series B: Physics*, edited by W. Greiner (Plenum, New York, 1987), p. 609.

[47] G. Mehler, G. Soff, K. Rumrich, and W. Greiner, Z. Phys. D **13**, 193 (1989).

[48] K. Rumrich, G. Soff, and W. Greiner, Phys. Rev. A **47**, 215 (1993).

[49] J. Hoffstadt, diploma thesis, Giessen, 1994.

[50] J. Thiel, J. Hoffstadt, N. Grün, and W. Scheid, Z. Phys. D **34**, 21 (1995).

[51] U. Becker, N. Grün, and W. Scheid, J. Phys. B **16**, 1967 (1983).

[52] C. Müller, diploma thesis, Giessen, 1994.

[53] J. C. Wells, V. E. Oberacker, A. S. Umar, C. Bottcher, M. R. Strayer, J. S. Wu, G. Plunien, Phys. Rev. A **45**, 6296 (1992).

[54] K. Momberger, N. Grün, W. Scheid, U. Becker, and G. Soff, J. Phys. B **20**, L281 (1987).

[55] A. H. Sǿrensen and A. Belkacem, Phys. Rev. A **49**, 81 (1994).

[56] K. T. R. Davies, H. Flocard, S. Krieger, and M. S. Weiss, Nucl. Phys. **A342**, 111 (1980).

[57] C. Bottcher, M. R. Strayer, A. S. Umar, and V. E. Oberacker, Phys. Rev. C **37**, 2487 (1988).

[58] C. Bottcher, M. R. Strayer, A. S. Umar, and P. G. Reinhard, Phys. Rev. A **40**, 4182 (1989).

[59] J. D. Bjǿrken and S. D. Drell, *Relativistic Quantum Mechanics* (McGraw-Hill, New York, 1964).

[60] J. D. Jackson, *Classical Electrodynamics*, 2nd ed. (Wiley, New York, 1975).

[61] J. McGuire and L. Weaver, Phys. Rev. A **16**, 41 (1977).

[62] J. F. Reading, Phys. Rev. A **8**, 3262 (1973).

[63] L. Kocbach, Z. Phys. A **279**, 233 (1976).

[64] M. Abramowitz and I. A. Stegun, *Handbook of Mathematical Functions* (Dover, New York, 1972).

[65] This code has been provided by Ben Feinberg (LBL) and is authored by Loren Meissner, 1965.

[66] W. H. Press, B. P. Flannery, S. A. Teukolski, and W. T. Vetterling, *Numerical Recipes* (Cambridge University Press, Cambridge, 1989).

[67] J. M. Feagin, *Quantum Mechanics with* MATHEMATICA (Springer Verlag, New York, 1994).

[68] M. E. Rose, *Relativistic Electron Theory* (Wiley, New York, 1961).

[69] H. J. Bär, G. Soff, Physica **128C**, 225 (1985).

[70] D. Trautmann, G. Baur, and F. Rösel, J. Phys. B **16**, 3005 (1983).

[71] I. S. Gradshteyn and I. M. Ryzhik, *Tables of Integrals, Series and Products* (Academic, New York, 1980).

[72] L. D. Landau and E. M. Lifschitz, *Quantum Mechanics, Non-Relativistic Theory*, 1st ed. (Pergamon, New York, 1958).

[73] L. F. Shampine and M. K. Gordon, *Computer Solutions of Ordinary Differential Equations: The Initial Value Problem* (Freeman, San Francisco, 1975).

[74] J. J. Sakurai, *Advanced Quantum Mechanics* (Addison-Wesley, Reading, MA, 1967).